Eur. Phys. J. D **17**, 57–66 (2001)

THE EUROPEAN PHYSICAL JOURNAL D

EDP Sciences

Multiphase patterns in self-phase-locked optical parametric oscillators

S. Longhi[a]

Istituto Nazionale di Fisica per la Materia, Dipartimento di Fisica and CEQSE-CNR, Politecnico di Milano, piazza L. da Vinci 32, 20133 Milano, Italy

Received 19 April 2001 and Received in final form 21 June 2001

Abstract. Multiphase patterns are found in a mean-field model of a singly-resonant optical parametric oscillator that converts a pump field at frequency 3ω into signal and idler fields at frequencies 2ω and ω. A complex Ginzburg-Landau equation without diffusion and with a quadratic phase-sensitive nonlinear term is derived under single-longitudinal and paraxial propagation approximations. Owing to the phase-matched multistep parametric process $\omega + \omega = 2\omega$, phase locking of the resonated signal field is possible with three distinct phase states. Three-armed rotating spirals, target patterns and light filamentation are found by a numerical analysis of the mean-field equation.

PACS. 42.65.Sf Dynamics of nonlinear optical systems; optical instabilities, optical chaos and complexity, and optical spatio-temporal dynamics – 42.65.Ky Harmonic generation, frequency conversion – 05.45.-a Nonlinear dynamics and nonlinear dynamical systems – 05.45.Xt Synchronization; coupled oscillators

1 Introduction

The formation of complex spatial and spatio-temporal structures in nonlinear optical systems has been the subject of an intensive research in the past few years [1–3]. Patterns as a result of a symmetry-breaking bifurcation have been predicted and observed in a wide variety of nonlinear optical systems, and major efforts have been paid toward a comprehensive and general description of these phenomena on the basis of universal pattern-forming mechanisms. Since the pioneering works by Oppo *et al.* and by Staliunas [4,5], much attention has been devoted to the study of optical patterns sustained by a quadratic ($\chi^{(2)}$) nonlinearity in the process of optical parametric oscillation (OPO) [4–12]. The extension of the earlier results to nondegenerate processes revealed at once a deep difference between pattern formation phenomena in degenerate *versus* nondegenerate processes [7,10]. The basic reason thereof stems from the fact that, in case of a degenerate OPO, signal and idler fields are indistinguishable both in frequency and polarization and the down-converted field is phase-locked to the pump field. Conversely, in a nondegenerate process signal and idler fields are usually not phase locked and their phase difference is free and may be subjected to, *e.g.*, stochastic fluctuations in presence of noise. This circumstance reflects the form of order parameter equations that describe pattern formation in the two cases: order-parameter equations with broken phase invariance for a degenerate OPO, such as parametrically-driven Ginzburg-Landau or real Swift-Hohenberg equations [6,8,9], phase invariant equations for a nondegenerate OPO, such as complex Ginzburg-Landau or complex Swift-Hohenberg equations [7,10,12].

From the point of view of optical patterns, the existence of phase locking in the degenerate OPO is appealing since, even in absence of any modulational instability, complex spatial structures and some form of localized states may occur owing to the coexistence, in different spatial domains, of two equivalent homogeneous states that differ each other by a π phase rotation. The formation of spatial structures in the phase-bistable degenerate OPO and the dynamics of domain walls that separate different phase-locked states have received indeed a great and increasing interest very recently, which major emphasis put toward the study of the dynamics of domain walls [13–18], the formation of labyrinth patterns [13] and of new types of localized structures [15,19–21]. Though the dynamics of two phase states is exclusive for a degenerate OPO, phase locking may occur as well in a special class of nondegenerate OPOs that convert a pump field at frequency 3ω into signal and idler fields at frequencies ω and 2ω [22–25]. Owing to the particular 1:2:3 ratios among signal, idler and pump waves, under suitable control of phase matching the multistep (degenerate) process $2\omega = \omega + \omega$ may simultaneously occur [26], which is responsible for phase locking [25]. As compared to the degenerate OPO, phase locking allows here for the existence of *three* different phase states, which are obtained each other by a $2\pi/3$

[a] e-mail: longhi@fisi.polimi.it

phase rotation. The plane-wave (temporal) dynamics of the self-phase-locked OPO in a doubly- or triply-resonant configuration has been recently investigated in reference [25], whereas pattern formation in these devices has been considered by the present author in references [27,28] in case of a weakly phase-matched multistep process. In particular, in reference [28] three-armed spiral waves have been shown to exist in a doubly-resonant OPO as a result of the phase tristability, and a 3ω parametrically-driven Ginzburg-Landau equation was derived to account for these structures.

In this paper we study the formation of multiphase patterns in a *singly–resonant* self-phase locked nondegenerate OPO, and show that, even without resonating the idler field, a rich variety of spatial and spatio-temporal structures, including three-armed spiral waves previously found for a doubly-resonant device, as well as new ones, can be observed. This is an important aspect from an experimental viewpoint, where simple configurations are more likely, as well as from a theoretical viewpoint, since the complex dynamical scenario found here is rather unusual for a singly-resonant device. The mean-field equation that describes the dynamics of the resonated signal field inside the cavity is shown to be a parametrically-driven Ginzburg-Landau equation, similar to that derived for the doubly-resonant configuration in reference [28] and generally found in 3ω parametrically-forced systems near an Hopf bifurcation [29–31], but with two distinctive aspects: the absence of diffusion, *i.e.* of wavenumber selection at the onset of instability, and the dependence of the quadratic phase-sensitive nonlinear term on the pump parameter.

The paper is organized as follows. In Section 2 the basic model and the mean-field equation of a singly-resonant OPO in the frequency divide-by-three configuration are detailed. In Section 3 the uniform solutions of the mean-field equation are derived and the phase locking-unlocking transition is discussed, together with a linear stability analysis of the phase-locked solutions. In Section 4 pattern formation is studied by numerical analysis of the mean-field equation and existence of rotating three-armed spiral waves, dynamic target patterns and complicated light filaments is pointed out. Finally, in Section 5 the main conclusions are outlined.

2 Mean-field model

We consider a simple model of a singly-resonant nondegenerate OPO, that consists of either a singly-ended monolithic cavity of length l, completely filled by a nonlinear $\chi^{(2)}$ medium [Fig. 1a], or of a ring cavity with planar mirrors [Fig. 1b], in which an injected plane-wave pump field at frequency 3ω is converted into signal and idler fields at frequencies ω and 2ω, respectively. The signal field is the only wave resonated inside the cavity, and T denotes the output power transmission of the output mirror at frequency ω. The injected plane-wave pump field of amplitude $\mathcal{E}$, as well as the generated idler field, escape from the cavity after one round-trip, as shown in Figure 1. The

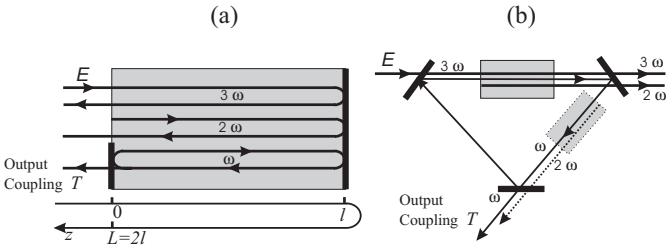

Fig. 1. Schematic of a singly-resonant OPO for the $3\omega \rightarrow 2\omega+\omega$ down-conversion process in a monolithic (a) and in a ring (b) cavity. In (a), the signal field at frequency ω is resonated while the pump and idler waves escape after one round-trip; the rear crystal face has high reflectivity for the three fields. In (b), pump and idler waves cross the crystal once; a second crystal for a further $\chi^{(2)}$ cascading process may be inserted in a second arm of the cavity (dashed curve).

nonlinear crystal is assumed to be phase matched for both the down conversion process $3\omega = \omega + 2\omega$ and for the multistep process $2\omega = \omega + \omega$. It should be noticed that, though simultaneous phase matching using birefringent techniques in a single crystal might be in practice a fortuitous circumstance, simultaneous and independent control of phase matching for the two processes can be achieved using nowadays available quasi phase-matching methods in two-section periodically-poled crystals or two separate crystals [24,32]. In the present work, we will assume perfect phase matching for the down-conversion process, *i.e.* $k(3\omega) = k(2\omega) + k(\omega)$, whereas we allow for a wavevector mismatch $\Delta k = k(2\omega) - 2k(\omega)$ for the multistep process, with a coherence length $l_c = \pi/\Delta k$ less than the interaction length. A mean-field equation for the normalized amplitude A_1 of resonated signal field, which accounts for diffraction effects in the paraxial approximation, can be derived using a standard technique, previously adopted for singly-resonant parametric devices [8,33], starting from the propagation wave equations for pump, signal and idler fields after the introduction of the single-longitudinal approximation and eliminating the not-resonated fields (*i.e.*, pump and idler waves) from the dynamics. In the spirit of the mean-field limit, the signal field suffers small change after each round-trip propagation, and its amplitude A_1 is assumed, at leading order, uniform along the cavity axis z. The mean-field equation then has the general form [33]:

$$\frac{\partial A_1}{\partial t} = \frac{\Delta A_1^{\mathrm{prop}} + \Delta A_1^{\mathrm{cav}}}{T_{\mathrm{R}}} \tag{1}$$

where $\Delta A_1^{\mathrm{prop}}$ and $\Delta A_1^{\mathrm{cav}}$ are the changes of intracavity signal field A_1 in one cavity round-trip due to propagation (diffraction and nonlinear wave interaction with pump and idler waves) and cavity effects (cavity losses and detuning), and T_{R} is the cavity round-trip time. The change in the intracavity field due to linear cavity losses and phase shift after one cavity round-trip is given by:

$$\Delta A_1^{\mathrm{cav}} = -\gamma T_{\mathrm{R}}(1 + \mathrm{i}\Delta)A_1 \tag{2}$$

where $\gamma = T/2T_{\mathrm{R}}$ is the cavity decay rate for signal field due to output coupling and $\Delta = (\omega_1 - \omega_c)/\gamma$ is

the normalized frequency detuning between the reference frequency ω_1 of signal field and the longitudinal cavity eigenfrequency ω_c closest to ω_1. The validity of equation (2) is ensured, as usual, provided that $T \ll 1$ and Δ be of order one, so that $\Delta A_1^{\rm cav}/A_1$ is small and of order $\sim T$. To determine the change of intracavity signal field due to round-trip propagation inside the crystal, we start with the paraxial wave equations describing interaction of pump, signal and idler fields for the simultaneous parametric processes $3\omega = 2\omega + \omega$ and $2\omega = \omega + \omega$, that read (see, for instance, [26]):

$$\frac{\partial A_1}{\partial z} = \frac{\rm i}{2k_1}\nabla^2 A_1 + gA_3A_2^* + \sigma A_1^* A_2 \exp(-{\rm i}\Delta k z) \quad (3a)$$

$$\frac{\partial A_2}{\partial z} = \frac{\rm i}{2k_2}\nabla^2 A_2 + gA_3A_1^* - \frac{\sigma}{2}A_1^2 \exp({\rm i}\Delta k z) \quad (3b)$$

$$\frac{\partial A_3}{\partial z} = \frac{\rm i}{2k_3}\nabla^2 A_3 - gA_1A_2 \quad (3c)$$

where: A_1, A_2, A_3 are normalized slowly-varying envelopes of signal, idler and pump waves; $k_l = k(\omega_l)$ $(l = 1, 2, 3)$ are the propagation wavevectors; $\Delta k = 2k_1 - k_2$ is the wavevector mismatch for the multistep process $2\omega = \omega + \omega$; g and σ are the nonlinear coupling coefficients for down-conversion and second-harmonic processes, respectively; and $\nabla^2 = \partial^2/\partial x^2 + \partial^2/\partial y^2$ is the transverse Laplacian. Equations (3) are coupled with the boundary conditions:

$$A_2(0,t) = 0, \quad A_3(0,t) = \mathcal{E}, \quad (4)$$

where $\mathcal{E}$ is the amplitude of incident pump field and $z = 0$ is assumed at the entrance face of the crystal. The incident pump field is assumed to be a plane-wave or a Gaussian or super-Gaussian beam with a flat phase at the entrance of the crystal and with a Rayleigh range $z_{\rm R}$ much greater than the crystal length l ($l/z_{\rm R} \sim O(T)$). The nonlinear coupled wave equations (3a, 3b, 3c) can be solved iteratively with the appropriate boundary conditions [Eq. (4)] assuming small pump conversion. To do that, it is worth introducing a right scaling for the fields and rewriting equations (3) in a dimensionless form suited for an iterative calculation [8]. For the sake of clearness, we will refer to the monolithic cavity of Figure 1a, although a similar analysis could be done for the ring geometry of Figure 1b. An inspection of the linear part of equations (3) without diffraction terms reveals that the parametric gain scales as $\sim (\mathcal{E}gL)^2$, where $L = 2l$ is the cavity length. Since the threshold condition is attained when $(\mathcal{E}gL)^2 \sim T$, $\mathcal{E}$ must be of order $\sim (\sqrt{T}/gL)$; this suggests us to set $A_3 = (\sqrt{T}/gL)B_3$, and to treat the dimensionless field envelope B_3 of $O(1)$. In order to determine the proper scaling for the fields A_1 and A_2, let us set $A_1 = (\sqrt{T}/gL)B_1T^{\alpha_1}$ and $A_2 = (\sqrt{T}/gL)B_2T^{\alpha_2}$, where the dimensionless amplitudes B_1 and B_2 are assumed to be of order ~ 1 and α_1, α_2 define the scaling of the fields and should be determined from an inspection of nonlinear terms in equations (3). From equation (3a) it follows that the change of B_1 in one round-trip due to nonlinear interaction with pump and idler waves is given by $\Delta B_1^{\rm NL} \sim T^{\alpha_2-\alpha_1+1/2}B_2^*B_3 + (\sigma/g)T^{\alpha_2+1/2}B_1^*B_2$, where the former contribution accounts for the down-conversion process whereas the latter one is due to the multistep process. In the spirit of the mean-field limit, we require that these two terms be small and of order $\sim T$. This yields $\alpha_1 = 0$ and $\alpha_2 = 1/2$. Finally, the spatial variables are scaled according to $z = LZ$, $x = bX$, $y = Yb$, where $b = (L/2k_1T)^{1/2}$ is the typical spatial scale of the patterns we will investigate. The chosen scaling for the transverse spatial variables is justified by the requirement that the field change due to diffraction in one cavity round-trip be of the same order of magnitude as that due to nonlinear $\chi^{(2)}$ interaction and cavity effects. With these appropriate scalings, equations (3) take the dimensionless form:

$$\frac{\partial B_1}{\partial Z} = {\rm i}T\nabla_X^2 B_1 + TB_3B_2^* + \frac{\sigma}{g}\exp(-{\rm i}\Delta kLZ)B_1^*B_2 \quad (5a)$$

$$\frac{\partial B_2}{\partial Z} = {\rm i}T\left(\frac{k_1}{k_2}\right)\nabla_X^2 B_2 + B_3B_1^* - \frac{1}{2}\frac{\sigma}{g}\exp({\rm i}\Delta kLZ)B_1^2 \quad (5b)$$

$$\frac{\partial B_3}{\partial Z} = {\rm i}T\left(\frac{k_1}{k_3}\right)\nabla_X^2 B_3 - TB_1B_2 \quad (5c)$$

with the boundary conditions:

$$B_2(0,t) = 0, \quad B_3(0,t) = \frac{\mathcal{E}gL}{\sqrt{T}}\,. \quad (6)$$

In the limit $T \to 0$, equations (5, 6) can be solved by a power expansion of B_1, B_2 and B_3 in powers of T. After setting $B_1 = B_1^{(0)} + TB_1^{(1)} + T^2B_1^{(2)} + ...$, $B_2 = B_2^{(0)} + TB_2^{(1)} + T^2B_2^{(2)} + ...$, $B_3 = B_3^{(0)} + TB_3^{(1)} + T^2B_3^{(2)} + ...$ in equations (5), a hierarchy of equations for successive corrections to B_1, B_2 and B_3 is obtained, which can be easily integrated. By pushing the expansion up to $O(T)$, one obtains for B_1 the following expression:

$$B_1(Z) = \psi + {\rm i}TZ\nabla_X^2\psi + |\mathcal{E}gL|^2Z^2\psi - \frac{\sigma}{2g}T\frac{\mathcal{E}gL}{\sqrt{T}}q_1(Z)\psi^{*\,2} - \frac{1}{2}\left(\frac{\sigma}{g}\right)^2 Tq_2(Z)|\psi|^2\psi + O(T^2), \quad (7)$$

where ψ is the scaled signal field envelope at $Z = 0$, and where we have set:

$$q_1(Z) = 3\frac{\exp(-{\rm i}\Delta kLZ) - 1}{(\Delta kL)^2} - Z\frac{1 + 2\exp(-{\rm i}\Delta kLZ)}{{\rm i}\Delta kL}, \quad (8a)$$

$$q_2(Z) = -{\rm i}\frac{Z}{\Delta kL} + \frac{1 - \exp(-{\rm i}\Delta kLZ)}{(\Delta kL)^2}\,. \quad (8b)$$

Notice that, for $\Delta kL \to 0$, one has $q_1(Z) = q_2(Z) \sim Z^2/2$. The change of signal field due to propagation in one cavity round-trip is then calculated as $\Delta A_1^{\rm prop} = (\sqrt{T}/gL)[B_1(1) - \psi]$; after re-introduction of the original

$$\rho = \frac{|Q_1|}{\sqrt{\mathrm{Re}(Q_2)}} = \left\{ \frac{[3\cos(\Delta kL) - 3 + 2\Delta kL\sin(\Delta kL)]^2 + [\Delta kL + 2\Delta kL\cos(\Delta kL) - 3\sin(\Delta kL)]^2}{(\Delta kL)^2[1-\cos(\Delta kL]} \right\}^{1/2}. \quad (15)$$

unscaled variables, it reads:

$$\Delta A_1^{\mathrm{prop}} = \mathrm{i}\frac{L}{2k_1}\nabla^2 A_1 + \frac{1}{2}g^2L^2|\mathcal{E}|^2A_1 + \frac{\sigma g}{2}L^2\mathcal{E}Q_1A_1^{*\,2} - \frac{\sigma^2L^2}{2}Q_2|A_1|^2A_1, \quad (9)$$

where we have set $Q_1 = q_1(1)$ and $Q_2 = q_2(1)$, *i.e.*:

$$Q_1 = 3\frac{\exp(-\mathrm{i}\Delta kL) - 1}{(\Delta kL)^2} - \frac{1 + 2\exp(-\mathrm{i}\Delta kL)}{\mathrm{i}\Delta kL}, \quad (10a)$$

$$Q_2 = -\mathrm{i}\frac{1}{\Delta kL} + \frac{1 - \exp(-\mathrm{i}\Delta kL)}{(\Delta kL)^2}\,. \quad (10b)$$

Notice that $\mathrm{Re}(Q_2) > 0$, *i.e.* the nonlinear cubic term in equation (9) is saturating, which justifies the truncation of the power expansion of the propagation equations (5) up to the order $\sim T$. Apart from diffraction effects represented by the Laplacian term, the right-hand side in equation (9) describes the change of signal field as a result of three cascading $\chi^{(2)}$ processes, which can be understood as follows. Photons at frequency ω are created by two distinct processes: down-conversion of the pump field, $\omega = 3\omega - 2\omega$, and degenerate down-conversion of idler field, $\omega = 2\omega - \omega$. The idler photons at frequency 2ω are in turn created by means of the two following processes: down-conversion of the pump, $2\omega = 3\omega - \omega$, and second-harmonic generation, $2\omega = \omega + \omega$. The cascading of these second-order processes then lead to the following four third-order processes, two of them being degenerate: $\omega = 3\omega - (3\omega - \omega)$, $3\omega - (\omega + \omega)$, $(3\omega - \omega) - \omega$, and $\omega + \omega - \omega$.

Using equations (2, 9), the mean-field equation (1) takes the final form:

$$T_{\mathrm{R}}\frac{\partial A_1}{\partial t} = -\gamma T_{\mathrm{R}}(1 + \mathrm{i}\Delta)A_1 + \mathrm{i}\frac{L}{2k_1}\nabla^2 A_1 + \frac{1}{2}g^2L^2|\mathcal{E}|^2A_1 + \frac{\sigma g}{2}L^2\mathcal{E}Q_1A_1^{*\,2} - \frac{\sigma^2L^2}{2}Q_2|A_1|^2A_1 \quad (11)$$

which is the main result of this section. Notice that the cubic saturating nonlinearity in equation (11) arises solely from the cascading process $\omega = \omega + \omega - \omega$, and no pump depletion effects enter in the equation. In addition, for a nonvanishing value of Δk, the cubic nonlinear term also possesses an imaginary part, either positive or negative, which is the usual Kerr effect due to $\chi^{(2)}$ cascading. The other cascading process $\omega = 3\omega - \omega - \omega$ leads to the appearance in the mean-field equation of a quadratic phase-dependent nonlinear term, which is responsible for self-phase locking of signal field. A simpler form for equation (11) can be derived after the change of variables $t \to t/\gamma$, $\nabla^2 \to (k_1T/L)\nabla^2$ and with a suitable rescaling of amplitude and phase of A_1 by setting $A_1(x,y,t) = \alpha u(x,y,t)\exp(\mathrm{i}\phi)$. In particular, since the phase of the injected pump wave $\mathcal{E}$ is assumed to be independent of transverse variables, the amplitude α and phase ϕ can be chosen such that the real part of the cubic nonlinear coefficient be equal to one and the coefficient of the quadratic nonlinear term be real and negative. This leads to the following canonical form for the mean-field equation:

$$\frac{\partial u}{\partial t} = -(1 + \mathrm{i}\Delta)u + \mu u + \mathrm{i}\nabla^2 u - \rho\sqrt{\mu}u^{*\,2} - (1 + \mathrm{i}\beta)|u|^2u, \quad (12)$$

where we have set:

$$\mu = \frac{(gL|\mathcal{E}|)^2}{T}, \quad (13)$$

$$\beta = \frac{\mathrm{Im}(Q_2)}{\mathrm{Re}(Q_2)} = \frac{\sin(\Delta kL) - \Delta kL}{1 - \cos(\Delta kL)}, \quad (14)$$

see equation (15) above.

In its present form, equation (12) is a parametrically-forced Ginzburg-Landau equation that describes the dynamics of a spatially-extended oscillatory system near a Hopf bifurcation when it is resonantly-forced at a frequency 3ω, where ω is its natural frequency [29–31], with μ playing the role of the pump (or bifurcation) parameter. A similar equation was recently derived by the author as an order parameter equation for the frequency divide-by-three OPO but in a *doubly–resonant* configuration, where both signal and idler waves are resonated in the optical cavity [28]. As compared to the previous analysis of reference [28], there are here a few distinctive aspects that is worth pointing out:

(i) the nonlocal (Laplacian) term in equation (12) is purely diffractive, and there is no mechanism for wavenumber selection in the linearized equation;
(ii) the form of equation (12) is valid regardless the sign of signal detuning Δ;
(iii) the coefficient of the quadratic phase-sensitive nonlinear term depends on the pump parameter μ;
(iv) saturation of the instability in equation (12) arises from the multistep process instead of from pump depletion.

As a final remark, notice that the coefficients ρ and β in equation (12) are not independent, but they are both determined once the wavevector mismatch Δk is assigned according to equations (14, 15). The behavior of ρ and β *versus* ΔkL is shown in Figure 2. Notice that the sign of ΔkL determines the sign of β in equation (12), *i.e.* the focusing ($\beta < 0$) or defocusing ($\beta > 0$) character of the third-order nonlinearity; notice also that the minimum of both ρ and $|\beta|$ is attained at perfect phase matching,

$$R = \frac{2(\mu-1)+\rho^2\mu-2\beta\Delta \pm \sqrt{\left(2\mu-2+\mu\rho^2-2\beta\Delta\right)^2-4(1+\beta^2)\left[\Delta^2+(\mu-1)^2\right]}}{2(1+\beta^2)} \tag{17}$$

$$\exp(3\mathrm{i}\phi) = \frac{\mu-1-R+\mathrm{i}(\Delta+\beta R)}{\rho\sqrt{R\mu}}\,. \tag{18}$$

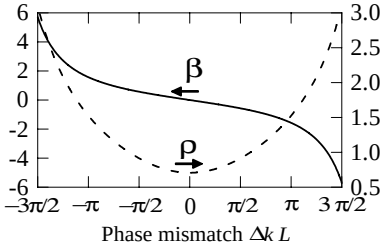

Fig. 2. Behavior of nonlinear coefficients β and ρ, entering in equation (12), *versus* ΔkL as given by equations (14, 15).

$\Delta kL = 0$, at which $\beta = 0$ and $\rho = 2^{-1/2}$. This means that nowhere in the parameter space the forcing quadratic nonlinear term in equation (12) may be assumed small. In some more complicated geometries, β and ρ may be however considered as independent parameters. This case occurs, for instance, when a not-pumped second nonlinear $\chi^{(2)}$ crystal, phase-matched for the second-harmonic process $\omega+\omega=2\omega$, is placed in a second arm of a ring cavity, as shown in Figure 1b. In this case, the role of the second crystal is to add, in equation (9), an additional cubic nonlinear term as a result of a cascading $\chi^{(2)}$ process, with a complex-valued coefficient that depends on the wavevector mismatch between signal and idler waves in the second crystal. In this work, we will be mainly concerned with the simplest case of the monolithic geometry of Figure 1a, where equations (14, 15) are valid.

3 Uniform states and their stability

The mean-field equation (12) admits of the trivial zero solution $u = 0$, corresponding to the OPO being below threshold, that becomes unstable at $\mu = \mu_{\rm th} = 1$ for a perturbation with any wavenumber k. Owing to the quadratic nonlinear term, the onset of instability is subcritical and the study of the dynamical development of instability above threshold is a highly nonlinear problem. Besides the trivial solution, the mean-field equation also possesses phase-locked homogeneous states, which exist and are stable in a wide range of parameter space (phase-locking regime). These states are given by:

$$u^{\pm}_{\rm ph} = \sqrt{R}\exp(\mathrm{i}\phi), \tag{16}$$

where R and ϕ are given by:

see equations (17, 18) above.

The double sign in equations (16, 17) defines two branches of phase-locked states. Notice that, according to equation (18), for a given branch there are *three* allowed values for the phase ϕ, which differ each other by a $2\pi/3$ phase rotation. The domain of existence of these phase-locked states is defined by the following inequality:

$$2(\mu-1)+\rho^2\mu-2\beta\Delta > \sqrt{4(1+\beta^2)\left[\Delta^2+(\mu-1)^2\right]}. \tag{19}$$

Within the domain of existence, one can easily determine the domain of stability by linearizing equation (12) around the fixed-point solution $u^{\pm}_{\rm ph}$. After setting $u = u^{\pm}_{\rm ph} + v_1\exp(\lambda t+\mathrm{i}\mathbf{k}\cdot\mathbf{r}) + v_2^*\exp(\lambda^* t-\mathrm{i}\mathbf{k}\cdot\mathbf{r})$, where $\mathbf{k}$ is the wavevector of perturbation, $\lambda=\lambda(k)$ its growth rate, $\mathbf{r}=(x,y)$, and v_1, v_2 small amplitudes, one obtains the following expression for the most unstable growth rate:

$$\lambda(k) = -1+\mu-2R + \sqrt{(2\mu-2-R)^2-(3\beta R+3\Delta+k^2)(\beta R-\Delta+k^2)} \tag{20}$$

where $k = |\mathbf{k}|$. An instability at wavenumber k arises whenever $\mathrm{Re}[\lambda(k)] > 0$. An inspection of equations (17, 20) reveals that the lower branch of phase-locked states, corresponding the lower sign in equation (17), is always unstable for a perturbation with zero wavenumber, and hence we will disregard in the following such branch. Depending on parameter values, the upper branch may be stable or show a modulational instability within a finite band of wavenumbers, with a most unstable wavenumber k_c lying inside the instability band. An example of bifurcation diagram for the phase-locked states, which assumes the pump parameter μ as the control parameter, is shown in Figure 3, together with the behavior of most unstable eigenvalue $\mathrm{Re}[\lambda(k_{\rm c})]$ and band of unstable wavenumbers around $k_{\rm c}$. The domains of existence and stability of the upper-branch phase-locked states largely depend on the three control parameters: the pump parameter, μ; the cavity detuning, Δ; and the phase mismatching parameter, ΔkL. As an example, Figure 4 shows the domains of existence and stability of the phase-locked states in the $(\mu,\Delta kL)$ plane for a few values of detuning parameter Δ.

For parameter values where the inequality (19) is not satisfied, there are not fixed point solutions to equation (12) and uniform solutions are oscillatory in time (limit cycles). As an example, Figure 5 shows the transition from oscillatory to phase-locked states assuming the cavity detuning Δ as the control parameter. The transition, which occurs at $\Delta=\Delta_{\rm c}\sim 0.7036$, is similar to the Andronov-van der Pol bifurcation [31,34], with stable and unstable phase-locked states merging as Δ approaches $\Delta_{\rm c}$ from below, giving rise to a limit cycle for $\Delta>\Delta_{\rm c}$ [see Fig. 5a]. For $\Delta\gg\Delta_{\rm c}$, the limit cycle is a circle (the one of the unforced complex Ginzburg-Landau equation), that

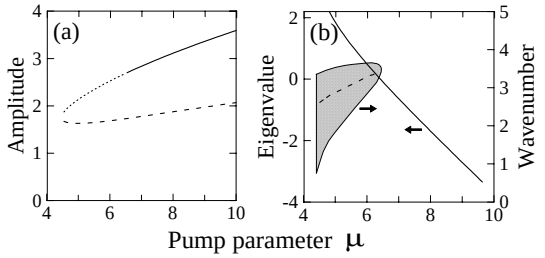

Fig. 3. (a) Normalized amplitude $R = |u|$ of phase-locked state *versus* pump parameter μ. The dashed curve is the (unstable) lower branch, the solid curve the (stable) upper branch, whereas the dotted curve is the modulationally unstable upper branch. Parameter values are: $\Delta kL = 1.879$ ($\rho = 1$, $\beta = -0.71$) and $\Delta = -1.5$. (b) Behavior of the real part of most unstable eigenvalue (solid curve) and corresponding perturbation wavenumber (dashed curve) versus pump parameter for the upper branch of (a). The phase-locked solution exists for $\mu \gtrsim 4.50$, whereas modulational instability occurs for $\mu \lesssim 6.52$. The shaded domain shows the band of unstable wavenumbers.

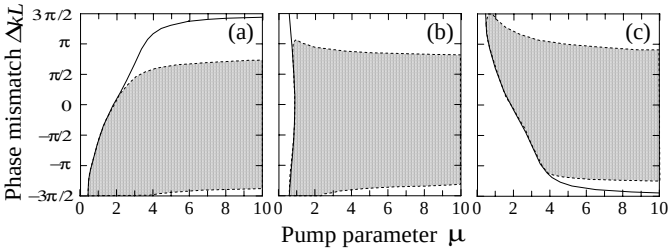

Fig. 4. Boundary of existence (solid curves) and stability domains (shaded areas) of the phase-locked solution in the $(\mu, \Delta kL)$ plane for a few values of detuning Δ. (a) $\Delta = -1$, (b) $\Delta = 0$, and (c) $\Delta = 1$. The domain of existence is on the right hand side of the solid curves.

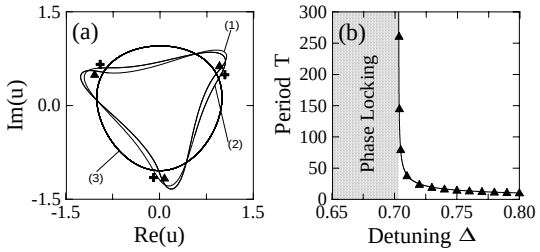

Fig. 5. (a) Uniform solutions of equation (12) in the phase space for a few values of cavity detuning Δ and for $\mu = 2$ and $\Delta kL = -1.879$ (corresponding to $\rho = 1$ and $\beta = 0.71$). The oscillatory regime occurs for $\Delta > \Delta_c$, with $\Delta_c \sim 0.7036$. The solid curves are the limit cycles corresponding to $\Delta = 0.76$ [curve (1)], $\Delta = 1$ [curve (2)] and $\Delta = 10$ [curve (3)]. Triangles and crosses correspond to stable and unstable fixed points, respectively, in the phase-locked regime for $\Delta = 0.65$. (b) Period T of oscillations as a function of cavity detuning in the oscillatory regime. Triangles refer to numerical simulations, whereas the solid line corresponds to a fitting curve $T = \kappa/(\Delta - \Delta_c)^{1/2}$, with $\kappa = 3.2$.

becomes deformed as Δ gets close to Δ_c [see Fig. 5a]. The period T of the oscillating state close to the transition point diverges as Δ approaches Δ_c from above with the typical law $T \sim (\Delta - \Delta_c)^{-1/2}$, as shown in Figure 5b. In addition, in the phase-locked regime with Δ close to Δ_c the system shows an excitable behavior, in the sense that small perturbations around a stable phase-locked state are damped, whereas large perturbations drive the system to another stable state through an heteroclinic trajectory [35].

The linear stability analysis of the uniform oscillatory states and the existence of pattern-forming instabilities in the oscillatory regime would require the determination of Floquet exponents $\lambda_\pm$ of the nonautonomous linear system obtained after linearization of equation (12) around the uniform oscillating solution. This analysis goes beyond the scope of the present work and will be not given here; however, we point out that, for large values of cavity detuning, $\lambda_\pm$ approach the eigenvalues $\lambda_\pm = -(\mu - 1) \pm \{(\mu - 1)^2(1 + \beta^2) - [k^2 + \beta(\mu - 1)]^2\}^{1/2}$ of the unforced complex Ginzburg-Landau equation, for which a Benjamin-Fair instability exists in the self-focusing case ($\beta < 0$) [35].

4 Pattern formation

The main pattern-forming properties of equation (12) are largely influenced by the existence of the quadratic phase-sensitive nonlinear term, that leads to self-phase locking of signal field in a wide range of parameter values. Such properties are common to the generic ones encountered in the problem of temporal forcing, at a frequency $n\omega$, of a spatially-extended system near a Hopf bifurcation, ω being the critical frequency of the Hopf bifurcation and n an integer number [29]. In these systems, the resonant forcing lead to the existence of n different phase-locked states, that may undergo a wide variety of bifurcations. For a sufficiently strong forcing, however, these states are linearly stable, and the formation of inhomogeneous structures, composed by domains of different locked states separated by domain boundaries, is possible. In particular, n-armed rotating spirals can be spontaneously formed, in which n different phase domains coalesce into a common point (vertex) and rotate around it. These properties have been investigated in great detail for the $n = 2$ and $n = 4$ cases, the former case in reference [29], the latter one in references [36,37]. The $n = 3$ resonant forcing case, which applies to our mean-field equation (12), was briefly considered in the earlier work by Coullet and Emilsson [29] and, more extensively, in few recent works [30,31]. In particular, in reference [31] the transition form the oscillatory to the excitable regime was studied in detail in case of exact resonant forcing, showing the transition from one-armed phase spirals to three-armed amplitude spirals, as well as the existence of other complex spatio-temporal structures. Although equation (12) has not, strictly speaking, the normal form considered in references [29,31], it is nevertheless expected to observe similar spatio-temporal structures [35]. We performed a numerical analysis of equation (12)

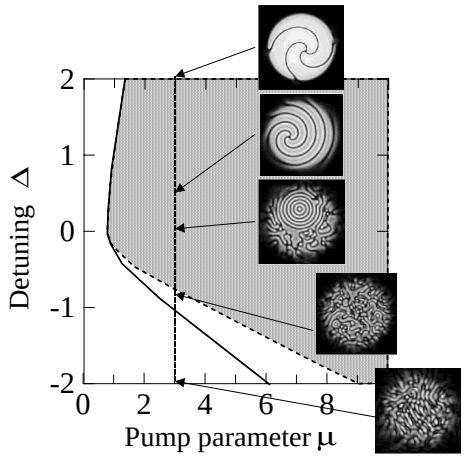

Fig. 6. Taxonomy of near-field intensity patterns of signal field in the self-focusing case ($\beta < 0$) as obtained by numerical simulations of equation (12). The shaded area in the (μ, Δ) plane is the stability domain of phase-locked states, whereas the solid curve is the boundary of existence of phase-locked states (they exist on the right side of the solid curve). The phase mismatch parameter is $\Delta kL = 1.879$, corresponding to $\rho = 1$ and $\beta = -0.71$.

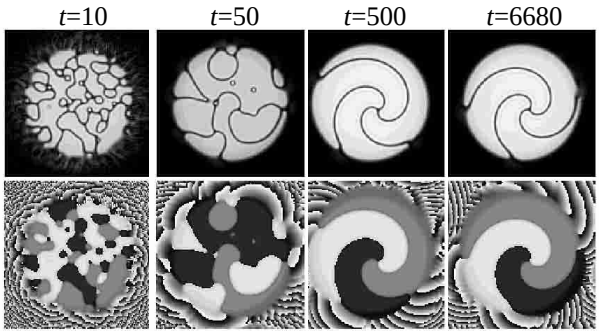

Fig. 7. Snapshots at successive times of intensity (upper row) and phase (lower row) of signal field showing the formation from noise of a rotating three-armed spiral wave for a super-Gaussian pump field ($w = 34$, $m = 4$, $\mu_0 = 3$) and for $\Delta = 2$. By decreasing the size of the pump beam down to $w = 20$, a homogeneous phase-locked state is obtained instead of a rotating spiral. The box size is 40×40 on a 128×128 spatial grid; time step: $\mathrm{d}t = 0.01$.

and revealed the existence of different dynamical regimes which are largely determined by the phase matching condition, *i.e.* by the value of ΔkL, and by the cavity detuning Δ. Our analysis is not intended to provide a comprehensive and definitive view of the taxonomy of the dynamics of equation (12) in the full parameter space, which is a rather ambitious and nontrivial task, instead it is aimed to show the richness of spatial and spatio-temporal dynamics that may occur in a self-phase-locked singly-resonant OPO device and to highlight the distinctive features of this device from the most studied two-phase bistable degenerate OPO. Equation (12) was numerically integrated using a split-step pseudospectral technique on a square domain with typical spatial grids of 128×128. The nonlocal term in the equation (diffraction) is calculated in the wavevector (Fourier) space whereas the linear and nonlinear local terms (pumping, detuning, nonlinear coupling) are computed in the space domain; a fast Fourier transform is used to shift from the space domain to the wavevector domain at each time step. A superGaussian axially-symmetric pump profile $\mu(x, y) = \mu_0 \exp[-(r/w)^{2m}]$ was assumed in the numerical analysis in order to simulate realistic OPO pumping conditions. A different dynamical scenario was observed depending on the sign of the phase mismatching term ΔkL, *i.e.* the focusing or defocusing character of the third-order nonlinearity in equation (12). A more complex behavior was found in the self-focusing case, which corresponds to the existence of the Benjamin-Fair instability for the unforced Ginzburg-Landau equation (see Sect. 3). Figure 6 shows schematically the taxonomy of typical intensity patterns in the self-focusing case ($\beta < 0$) that spontaneously arise starting from a small noise added to the zero solution for fixed values of the pump parameter μ_0 and wavevector mismatch ΔkL when the cavity detuning Δ is varied; in the figure are also shown the boundary of existence (solid curve) and domain of stability (shaded area) of the phase-locked states in the (μ, Δ) plane for a flat pump. Numerical simulations show that phase-locked states with different phases spontaneously grow from noise in different spatial regions and rapidly saturate the initial instability; since the phase-locking mechanism is nonlinear, the process of phase-locking and saturation of instability act simultaneously. Domain walls, that connect different phase domains, appear as dark lines in the field intensity, and their evolution may lead to different dynamical scenarios depending on cavity detuning. For positive and large values of detuning inside the stability domain of phase-locked states, shrink or expansion of domain walls, leading to a one dominating final phase-locked state, is observed; as the detuning is decreased, different domains coalescing in one point tend to rotate around it, and the system show the spontaneous formation of three-armed rotating spiral waves. Annihilation of counter-rotating spirals is observed and, after some transient, the final state typically comprises, within the integration domain, solely one rotating spiral. Figures 7 and 8 show in detail the formation from noise of three-armed rotating spirals for two values of cavity detuning; the frames plot the intensity and phase of the signal wave in the near-field at successive times. As the detuning is decreased from $\Delta \sim 2$ (Fig. 7) to $\Delta \sim 1$ (Fig. 8), the curvature of spiraling domains increases, which allows to accommodate spiral waves in narrower integration domains. Indeed, if the pump size in Figure 7 were decreased, a single homogeneous phase-locked state, instead of a spiral wave, would have been the final attractor. As the cavity detuning is further decreased, the tendency of different domains to spiral vanishes, instead spontaneous nucleation of target patterns, composed by annular domains of alternating phase-locked states, is observed, as shown in Figure 9. Target patterns are not in a stationary state, instead continuous nucleation of a new phase-locked state at the center of the structure, which

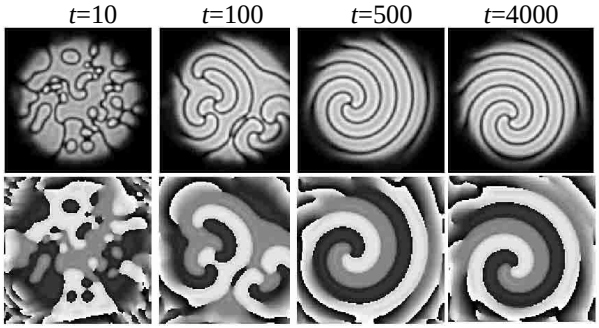

Fig. 8. Same as Figure 7 but for $\Delta = 0.5$. The pump size is $w = 18.7$; the box size is 22×22 on a 128×128 spatial grid; time step: $\mathrm{d}t = 0.005$.

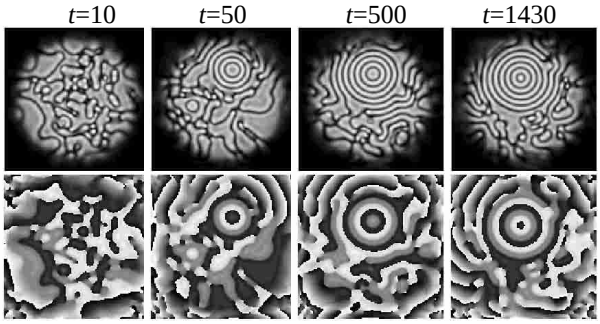

Fig. 9. Same as Figure 8, but for $\Delta = 0$.

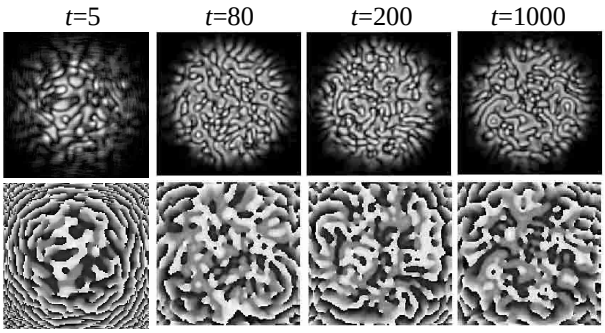

Fig. 10. Same as Figure 8, but for $\Delta = -0.8$.

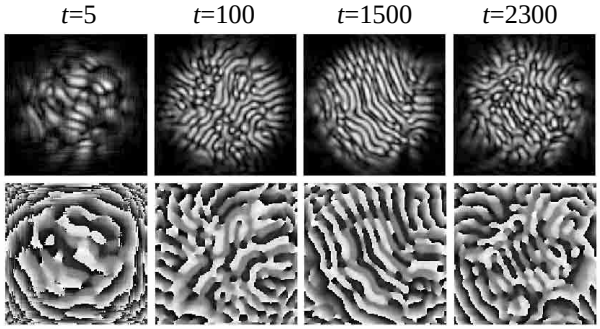

Fig. 11. Same as Figure 8, but for $\Delta = -2$.

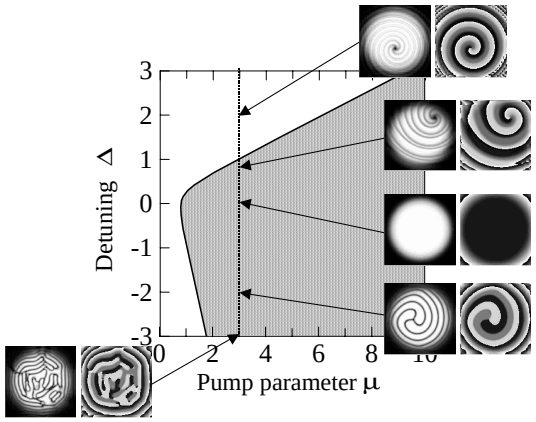

Fig. 12. Taxonomy of intensity and phase patterns of signal field in the self-defocusing case ($\beta > 0$) as obtained by numerical simulations of equation (12) assuming a superGaussian pump ($\mu_0 = 3$, $w = 18.7$, $m = 4$) and for $\Delta kL = -1.879$, corresponding to $\rho = 1$ and $\beta = 0.71$. The shaded area in the (μ, Δ) plane is the stability domain of phase-locked states.

moves toward the boundary, is typically observed. As the detuning is further decreased, target patterns with less regular structure are spontaneously nucleated in different spatial regions of the integration domain, and they seem to interact and evolve in an erratically way. As the detuning is decreased to cross the stability boundary of Figure 6, a complex spatio-temporal dynamics is observed, with the continuous nucleation and annihilation of bubbles and the formation of labyrinth structures (see Fig. 10). The complex spatial structures in the near-field is accompanied, in the far-field, with the excitation of a broad band of wavevectors around $k = 0$, which is a signature of the complex spatio-temporal dynamics. At further low values of detuning to cross the oscillatory boundary, the formation of disordered light filaments, which evolve erratically in time, is observed which resembles the turbulent regimes of the corresponding unforced Ginzburg-Landau equation (see Fig. 11).

In the self-defocusing case ($\beta > 0$), the Benjamin-Fair instability is prevented and the dynamics is less variegated. A typical taxonomy of intensity and phase patterns, at a fixed value of pump parameter and for a few values of cavity detuning, is schematically shown in Figure 12. In this case, as opposed to that of Figure 6, the domains of existence and stability of the phase-locked states are coincident. A superGaussian pump was used in the simulations, with a pump size $w = 18.7$ and a superGaussian order $m = 4$ as in Figure 6. For positive values of detuning outside the phase-locking domain ($\Delta = 2$ in the figure), amplitude spirals appear in the signal intensity, though phase locking is not effective. Such structures resemble the phase spiral defect dynamics of the corresponding Ginzburg-Landau equation without forcing, and the occurrence of dark lines in the field amplitude is due to the weak forcing term. As the detuning is decreased, the split of the phases into three locked states is observed

approximately when crossing the phase-locking stability boundary. In this case, domains of different phase states typically shrink or expand, and vertex annihilation is observed, until a final homogeneous phase-locked state is observed (see the frames in Fig. 12 corresponding to $\Delta = 0$). It should be noticed that, close to the stability boundary, stable amplitude spirals may be still observed, but at the boundary of the pumping region (see, *e.g.*, the frames in Fig. 12 corresponding to $\Delta = 0.7$). The stabilization mechanism is probably due to a boundary effect, related to the relatively slow decay of pumping in the outer region, where the lower forcing does not induce phase locking and defect phase dynamics similar to that occurring in the unlocking case is possible. By decreasing the value of detuning, three-armed spirals, in which three domains of different phases coalesce into a vertex and rotate around it, are observed (see the frames in Fig. 12 corresponding to $\Delta = -2$). At lower values of detuning, a more complex dynamics of domain walls is observed (see the frames in Fig. 12 corresponding to $\Delta = -3$), which does not settle down into a quiescent state.

As a final note, let us briefly discuss the experimental feasibility of observing multiphase patterns in a singly-resonant self-phase-locked OPO. Let us consider, as an example, parametric down conversion of a pump field at wavelength $\lambda_{3\omega} = 532$ nm in a periodically-poled lithium niobate crystal with a double grating (see, *e.g.*, Ref. [32]) and with plane faces dielectrically coated to provide a high finesse cavity for the signal field ($\lambda_\omega = 1596$ nm). The three fields are assumed to be extraordinary waves and first-order quasi phase-matching is assumed for the process $3\omega \to 2\omega + \omega$, with an effective nonlinear coefficient $d_{\rm eff} = 2d_{33}/\pi \sim 21$ pm/V for lithium niobate. In physical units, the intensity $I_{3\omega}$ of the pump wave is related to the bifurcation parameter μ entering in equation (12) through the relation $I_{3\omega} = \mu(\epsilon_0 c_0^3 T n_1 n_2/(16 l^2 d_{\rm eff}^2 \omega^2)$, where: $\epsilon_0 = 8.854 \times 10^{-12}$ C^2/N m^2 is the vacuum dielectric constant; $c_0 = 3 \times 10^8$ m/s is the speed of light in vacuum; $n_1 = 2.137$ and $n_2 = 2.176$ are the extraordinary refractive indices at signal and idler wavelengths; T is the output mirror transmission; and l is the crystal length. The spatial scale of patterns is given by $L_{\rm spatial} = [l\lambda_\omega/(\pi T n_1)]^{1/2}$. Assuming, for instance, $T = 5\%$ and $\mu = 3$, a pump intensity $I_{3\omega} \sim 17$ kW/cm^2 and a spatial scale $L_{\rm spatial} \sim 488$ μm are obtained. For a Gaussian pump with scaled parameters $\mu_0 = 3$ and $w_0 = 18$, which applies to the simulations shown in Figures 6 and 12, a pump beam size $W_0 = w_0 L_{\rm spatial} \sim 8.8$ mm and a pump power level $P_{3\omega} = \pi W_0^2 I_{3\omega} \sim 40$ kW are obtained. Such a high pump level might be available using a pulsed pump beam, with a pulse duration of $\sim$ 100–200 ns which is enough for the formation of patterns.

5 Conclusions

In conclusion, a mean-field model of a singly-resonant nondegenerate OPO in the frequency divide-by-three configuration has been presented, and a new class of patterns, that result from the self-phase locking of signal field induced by a multistep parametric process, have been found. These patterns belong to the general class of resonant patterns found in temporal forcing of spatially-extended systems near a Hopf bifurcation, and hence bear a close connection with similar structures recently observed and studied in some detail in periodically-forced chemical systems [36–38]. The present analysis suggests that the class of self-phase locked OPOs, even when a singly-resonant configuration is employed, may provide a rich framework in nonlinear optics to study complex pattern formation for the $n = 3$ resonant forcing regime which has been until now considered mostly in other fields of science.

This research was supported in part by the "Progetto Giovani Ricercatori" and by the ESF Network PHASE.

References

1. L.A. Lugiato, M. Brambilla, A. Gatti, *Optical Pattern Formation*, in: Adv. At. Mol. Opt. Phys. **40**, edited by B. Bedersen, H. Walther (Academic Press, Boston, 1998).
2. Special issue on *Patterns in Nonlinear Optical Systems*, edited by G. de Valcarcel, E. Roldan, R. Vilaseca, Quant. Semiclass. Opt. **10**, 775 (1998); J. Opt. B: Quant. Semiclass. Opt. **1**, 1 (1999).
3. F.T. Arecchi, S. Boccaletti, P. Ramazza, Phys. Rep. **318**, 1 (1999).
4. G.-L. Oppo, M. Brambilla, L.A. Lugiato, Phys. Rev. A **49**, 2028 (1994); G.-L. Oppo, M. Brambilla, D. Camesasca, A. Gatti, L.A. Lugiato, J. Mod. Opt. **41**, 1151 (1994).
5. K. Staliunas, J. Mod. Opt. **42**, 1261 (1995).
6. G.J. De Valcarcel, K. Staliunas, E. Roldan, V.J. Sanchez-Morcillo, Phys. Rev. A **54**, 1609 (1996).
7. S. Longhi, Phys. Rev. A **53**, 4488 (1996).
8. S. Longhi, J. Mod. Opt. **43**, 1089 (1996).
9. S. Longhi, A. Geraci, Phys. Rev. A **54**, 4581 (1996).
10. V.J. Sanchez-Morcillo, E. Roldan, G.J. De Valcarcel, K. Staliunas, Phys. Rev. A **56**, 3237 (1997).
11. M. Santagiustina, P. Colet, M. San Miguel, D. Walgraef, Opt. Lett. **23**, 1167 (1998).
12. Z.H. Musslimani, Physica A **249**, 141 (1998).
13. K. Staliunas, V.J. Sanchez-Morcillo, Phys. Lett. A **241**, 28 (1998).
14. N. Kutz, T. Erneux, S. Trillo, M. Haeltermann, J. Opt. Soc. Am. B **16**, 1936 (1999).
15. G.-L. Oppo, A.J. Scroggie, W.J. Firth, J. Opt. B **1**, 133 (1999).
16. M. Tlidi, P. Mandel, M. Le Berre, E. Ressayre, A. Tallet, L. Di Menza, Opt. Lett. **25**, 487 (2000).
17. G. Izus, M. San Miguel, M. Santagiustina, Opt. Lett. **25**, 1454 (2000).
18. G.-L. Oppo, A. Scroggie, W.J. Firth, Phys. Rev. E **63**, 066209 (2001).
19. S. Trillo, M. Haeltermann, A. Sheppard, Opt. Lett. **32**, 970 (1997); S. Longhi, Phys. Scripta **56**, 611 (1997).
20. K. Staliunas, V.J. Sanchez-Morcillo, Phys. Rev. A **57**, 1454 (1998); V.J. Sanchez-Morcillo, K. Staliunas, Phys. Rev. E **60**, 6153 (1999).
21. M. Le Berre, D. Leduc, E. Ressayre, A. Tallet, J. Opt. B **1**, 153 (1999).

22. A. Douillet, J.-J. Zondy, Opt. Lett. **23**, 1259 (1998).
23. A. Douillet, J.-J. Zondy, A. Yelisseyev, S. Lobanov, L. Isaenko, J. Opt. Soc. Am. B **16**, 1481 (1999).
24. K. Boller, R. Wallenstein, J.-P. Mayn, D.-H. Lee, M. Klein, P. Grob, Opt. Expr. **5**, 114 (1999).
25. J.-J. Zondy, A. Douillet, A. Tallet, E. Ressayre, M. Le Berre, Phys. Rev. A **63**, 023814 (2001).
26. K. Koynov, S. Saltiel, Opt. Commun. **152**, 96 (1998); Y.S. Kivshar, T.J. Alexander, S. Saltiel, Opt. Lett. **24**, 759 (1999).
27. S. Longhi, Opt. Lett. **26**, 713 (2001).
28. S. Longhi, Phys. Rev. E **63**, 055202(R) (2001).
29. P. Coullet, K. Emilsson, Physica D **61**, 119 (1992).
30. C.J. Hamming, R. Kapral, Chaos **10**, 720 (2000).
31. R. Gallego, D. Walgraef, M. San Miguel, R. Toral, "Transition from oscillatory to excitable regime in a system forced at three times its natural frequency", unpublished.
32. P.T. Nee, N.C. Wang, Opt. Lett. **23**, 46 (1998).
33. P. Lodahl, M. Saffman, Phys. Rev. A **60**, 3251 (1999).
34. D. Walgraef, *Spatio-Temporal Pattern Formation* (Springer, New York, 1997).
35. The main properties of the parametrically-forced Ginzburg-Landau equation, including the existence of pattern-forming instabilities, the excitable behavior and the divergence of the period of limit cycle near the phase locking-unlocking transition, have been analytically described in references [29,31,34] by derivation of appropriate phase equations, which is possible in the limit of small forcing. Though for our system the forcing can not be made small (see Fig. 2) and the phase approximation not invoked, the behavior found by numerical analysis shows the generic features valid within the phase approximation.
36. C. Elphick, A. Hagberg, E. Meron, Phys. Rev. Lett. **80**, 5007 (1998); Phys. Rev. E **59**, 5285 (1999).
37. A.L. Lin, M. Bertram, K. Martinez, H.L. Swinney, A. Ardelea, G.F. Carey, Phys. Rev. Lett. **84**, 4240 (2000); A.L. Lin, A. Hagberg, A. Ardelea, M. Bertram, H.L. Swinney, E. Meron, Phys. Rev. E **62**, 3790 (2000).
38. V. Petrov, Q. Ouyang, H.L. Swinney, Nature **338**, 655 (1997).